Int. J. Electrochem. Sci., 8 **(2013)** 12816 - 12836

International Journal of
ELECTROCHEMICAL
SCIENCE
www.electrochemsci.org

Scale-up synthesis, Structure Characterization and Electrochemical Characteristics of C-$LiFePO_4$ Nanocomposites for Lithium Ion Rechargeable Batteries

Xiangcheng Sun[1,*], *Kai Sun*[2], *Yongqing Wang*[3], *Xuedong Bai*[4], *Caiyun Chen*[5], *and Bo Cui*[1]

[1]Department of Electrical and Computer Engineering, University of Waterloo, Waterloo, Canada
[2]Department of Materials Science and Engineering, University of Michigan, Ann Arbor, Michigan, USA
[3]Institute of Chemistry, Chinese Academy of Sciences, Beijing, China
[4]Institute of Physics, Chinese Academy of Sciences, Beijing, China
[5]College of Physics Sciences, Qingdao University, Qingdao, China
[*]E-mail: sunxc824@gmail.com

Received: 28 July 2013 / *Accepted:* 5 September 2013 / *Published:* 20 October 2013

Carbon-coated $LiFePO_4$ (C-$LiFePO_4$) nanocomposites particles have been scale-up synthesized by a direct and economic solid-state reaction process. A variety of analytical techniques such as X-ray diffraction (XRD), scanning and transmission electron microscopy (SEM, TEM, HRTEM, and HAADF), and selected area electron diffraction (SAED) are applied to investigate particles morphologies and phase structures on the nanometer scale. Single crystal and an olivine structure of the rough spherical $LiFePO_4$ are confirmed by XRD pattern, HRTEM images and SAED patterns. The details of the coating including carbon content, thickness, and structure are particularly studied by energy filtered EF-TEM imaging, electron energy-loss spectroscopy (EELS) analysis, and X-ray photoelectron spectroscopy (XPS) analysis. The size distribution is estimated at 50-200 nm from XRD analysis and TEM images. An average 4.2% carbon content is measured and a homogenous 3 nm carbon thick layer on the particles surfaces is clearly revealed by HRTEM and EF-TEM imaging. An amorphous carbon structure was further confirmed by both EELS and XPS valence analysis. The characteristics of these nanostructures and the amorphous carbon-coating has been demonstrated to improve the electronic conductivity and cell performance by reducing the path of both electron transfer and lithium ions diffusion while the C-$LiFePO_4$ cathode is used in the battery cell. Electrochemical performance has been evaluated by cyclic voltammetry (CV), and galvanostatic charge/discharge cycling, and AC impedance spectroscopy (EIS). The C-$LiFePO_4$ particles exhibited improved electric conductivity, good rate capability, capacity retention, and cycling performance and superior discharge capacity with delivery of almost 99% of its theoretical discharge capacity of 168 mAh/g at a C/10 rate with a high coulomb efficiency. The CV profiles show that lithium ions and electrons are quite active during two-phase kinetic reaction, which could be attributed to the smaller particles and carbon-coating layer that facilitated extraction and insertion of lithium ions and electrons transfers, thereby is beneficial to the kinetic behavior and improving electrochemical performance during charge-discharge

processes. This investigation showed that the low cost and direct solid-state manufacturing process can produce the active $LiFePO_4$ cathode for the development of high-power Li-ion batteries for hybrid electric vehicles.

Keywords: $LiFePO_4$, carbon coating, transmission electron microscopy, cyclic voltammetry, electrochemical kinetic reaction

1. INTRODUCTION

In the past decade, considerable attention has been extensively devoted to the phospho-olivine type lithium iron phosphate ($LiFePO_4$) for use as an attractive and promising cathode candidate, which was first reported as a cathode electrode for rechargeable lithium-ion batteries in 1997 by John Goodenough and co-workers [1]. Olivine-type $LiFePO_4$ exhibits various unique advantages such as low toxicity, low cost, high thermal and chemical stability, and good electrochemical performance in the fully charged state. Particularly, though it shows a slightly lower voltage than the widely used commercial lithium metal oxides with either a layered structure ($LiMO_2$, M = Co, Ni) or a spinel structure (LiM_2O_4, M = Ni, Mn) cathode, it has a higher theoretical specific capacity (170 mAh/g) and a flat charge–discharge profile at intermediate voltage (3.45 V vs Li/Li^+), and reasonable cycle life [2-3].

Basically, orthorhombic $LiFePO_4$ has an ordered olivine structure, and has a relatively larger theoretical capacity of 170 mAh/g compared with other iron-based compounds [1]. $LiFePO_4$ crystal is in the Pnma space group, and consists of distorted LiO_6, FeO_6, and PO_4 units. The cation arrangement in $LiFePO_4$ differs significantly from that in layered or spinel structures. The strong covalent bonding between the oxygen and P^{5+} to form the $(PO_4)^{3-}$ unit allows for greater stabilization in such structures compared to the layered oxides [2]. However, there is no continuous network of FeO_6 edge-shared octahedra that might contribute to the electronic conductivity. Instead, the divalent Fe^{2+} ions occupy the corner-shared octahedra. The P^{5+} is located in tetrahedral sites, and Li^+ resides in chains of edge-shared octahedra [1]. Therefore, $LiFePO_4$ has inherently low electronic conductivity (10^{-9} to 10^{-10} S cm^{-1}), which results in its poor rate capability due to the poor kinetics of the lithium intercalation/de-intercalation process [2-4], so that it poses a great challenge for power-demanding applications such as hybrid electric vehicles and electric vehicles [5, 6].

Among the characteristics of cathode materials, their electronic conductivity and lithium ion diffusion coefficient are two of the most important issues responsible for the rate capability of batteries.

General, highly conductive carbon additives like carbon black or graphite are often added during the battery cell manufacturing process into active materials with a binder to enhance the conductivity of the cathode electrodes [5]. While, the particle size of $LiFePO_4$ cathode becomes smaller, down to the nanometer, a large proportion of carbon additive is required to connect all active materials, which causes low loading of active materials. Therefore, effective dispersion of carbon additives with active $LiFePO_4$ cathode is also a challenge.

So far, many nano-engineering approaches and/or attempts have been pursued and implemented to overcome its poor conductivity and improve the electrochemical performance of olivine-type $LiFePO_4$, such as metal cation or anion ion doping [7, 8], and carbon-coating [9-19], and/or by controlling off-stoichiometric Fe/P/O compositions [20], and/or by using smaller particle sizes that could shorten the diffusion length of Li-ion [14-18].

It was found that the conductivity can be effectively improved by creating such a conductive carbon coating layer on the $LiFePO_4$ particles at the nano-scale, usually bearing carbon in the amount of less than 2 wt%. The electrons can be spread to the entire surface of the particles through this carbon layer during charge/discharge and the layer therefore improves the kinetics and reversibility of the lithium intercalation/de-intercalation cycles and gives rise to enhanced rate capability [7-19]. In fact, the most effective way to increase the conductivity with a minimal weight missing is to apply such a carbon coating on the $LiFePO_4$ particle surface during solid-state or gas-phase synthesis using the carbon precursors [21]. A thin layer of carbon can be formed simultaneously on the pristine $LiFePO_4$ surface during solid-state synthesis [21] or by the carbonization of the organic materials in solution at the elevated temperature [22].

In this study, we present the larger scale synthesis, structural morphology and electrochemical characterization of C-$LiFePO_4$ material prepared by a direct solid phase reaction method using home-made amorphous micro-$FePO_4$ as the iron source and conducting black. Furthermore, this method using micro-$FePO_4$ as the starting material is cheap and environmentally benign for the potential mass production of carbon coated phospho-cathode (i.e. $LiMPO_4$, M = Fe, Co) materials, compared with other starting materials of divalent iron such as $(CH_3COO)_2Fe$, which are expensive and toxic. In addition, the synthesis method we presented here does not need any additional treatments, such as ball-milling and pre-sintering treatments necessary for the traditional solid-state reaction routine [23].

2. EXPERIMENTAL SECTIONS

2.1. Solids-state synthesis

In order to prepare the homogenous carbon-coated $LiFePO_4$ cathode material, selecting the proper synthetic procedure is very important. Otherwise, undesired impurities such as Fe_2O_3, Fe_2P and Li_3PO_4 can be contained in the final products [9, 20]. Our present C-$LiFePO_4$ particles were scale-up produced through a two-step solid state reaction using the cheap raw materials powders mixing of iron(II) oxalate [$Fe(C_2O_4)\cdot 2H_2O$], ammonium di-hydrogen phosphate [$NH_4H_2PO_4$] and lithium carbonate [Li_2CO_3] in the appropriate stoichiometry of molar ratio and acetylene black. All the reagents used in the experiment are of analytical purity. Generally, in a typical synthesis, the prepared powder mixtures are treated by a high temperature solid state reaction and carried out under controlled high temperature and pressure.

2.2. First-step synthesis of micro-$FePO_4$ powders

The first step (pre-calcination) was the solid state synthesis of micro-$FePO_4$ powders, which was typically carried out by heating the mixture of precursors of $Fe(C_2O_4)\cdot 2H_2O$ and $NH_4H_2PO_4$ (the

molar ratio of $Fe(C_2O_4)\cdot 2H_2O$ and $NH_4H_2PO_4$ is 1:2) at 250 - 350^oC, which was designed for the decomposition of the precursors and expelling of the gases. After heat treated and dried for 10-15 h, yellowish-white amorphous micro-$FePO_4$ powders were obtained by direct-mass production.

2.3. Second-step synthesis of C-LiFePO$_4$ nanocomposites

The second step is the final calcination of appropriate stoichiometric amounts of amorphous micro-$FePO_4$ powders and Li_2CO_3, and the conductive carbon source (i.e. acetylene black) in an industrial-type furnace, which occurred at relatively high temperatures (e.g., 800^oC). The calcinations temperature has an important effect on the resultant structure and particle size (particle growth) [24]. Finally, the sample is cooled to room temperature for the resultant products. The resultant C-$LiFePO_4$ powders, with the particle sizes ranging in 50-100 nm (the aggregates are up to1 μm), can be obtained by directly adjusting stoichiometric amounts of all the precursors under different temperatures and pressures.

2.4 Structure characterization and phase analysis

Firstly, the phase and size distribution of the C-$LiFePO_4$ particles were analyzed by powder X-ray diffraction (XRD) using a D/max−2000 Rigaku diffractometry with Cu Kα radiation (λ = 0.15406 nm) operated at 40 kV and 30 mA.

Secondly, the particles surface morphology was examined by a Hitachi S-4800 field-emission scanning electron microscopy (FE-SEM) equipped with an energy-dispersive X-ray spectroscopy detector. Crystallographic structure, phase structure and characteristics of the carbon coating were evaluated and recorded by transmission electron microscopy (TEM), and high-resolution transmission electron microscopy (HR-TEM), and selected area electron diffraction (SAED) techniques on particles supported on a 200 mesh Cu grid at 300 kV in the JEOL 3010 microscope equipped with a Gatan image filter (GIF) spectrometer.

Thirdly, energy filtered TEM (EF-TEM) imaging, high-angle annular dark field (STEM - HAADF) imaging and elemental mapping, and electron energy-loss spectroscopy (EELS) analysis were carried out on particles in STEM mode by the JEOL 2010F AEM using a probe size of 0.2 nm. The STEM-EELS spectra were recorded in diffraction (image coupled) mode with an energy resolution of ~ 1.1 eV, as measured by the full width at half-maximum of the zero-loss peak (ZLP). After acquisition, all spectra were first gain- and dark-count-corrected and then deconvolved by the ZLP with the EELS program.

Fourthly, the surface chemical elements measurements were determined by X-ray photoelectron spectrometer (XPS) using a Kratos ULTRA DLD XPS with a mono-chromated Al source that gives an energy resolution better than 0.5 eV. The binding energy scale was calibrated by setting the P peak as the inner standard.

2.5 Electrochemical testing

Electrochemical properties were measured on the electrodes prepared using the mixtures comprised of 80 wt% active material, 10 wt% acetylene black, and 10 wt% polyvinylidene fluoride (PVDF) binder. The $LiFePO_4$ nanocomposites electrode films were fabricated by the doctor blade technique on aluminum foil and dried in a vacuum oven at 100^oC for 10 h. The cells consisted of the electrode, a lithium metal counter electrode and the electrolyte of a 1M solution of $LiPF_6$ in ethylene carbonate/dimethyl carbonate (EC/DMC, 1:1). The cells were assembled and handled in an Ar-filled glove box and were evaluated using CR 2032 coin-type cells.

Galvanostatic charge-discharge cycling tests for the cells were performed within a range of 2.0V-4.2V versus the Lithium counter electrode (versus Li^+/Li) in an Arbin BT2000 battery test system. The specific capacities of the measured samples were calculated based on the mass of the composites. The cyclic voltammetry (CV) was performed by the scan rate of 0.1 mV/s between 2.0V and 4.5V, and electrochemical impedance spectroscopy (EIS) was carried out on the coin cells in the fully charge state at the frequency range between 100 kHz and 10 mHz.

3. RESULTS AND DISCUSSION

3.1 Morphology and structure characterization

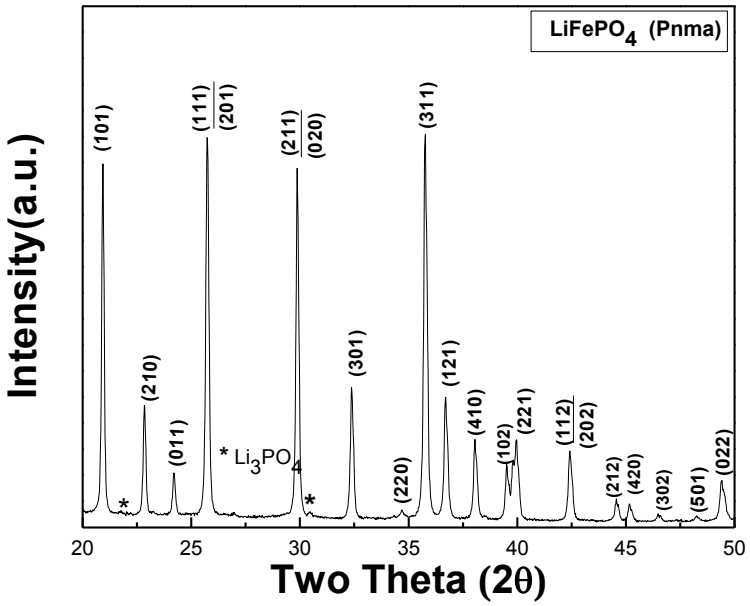

Figure 1. Powder XRD pattern indexed with Olivine structure for the C-$LiFePO_4$ nanocomposites. The reflections marked with * refer to the impurity phase, Li_3PO4.

The structure and size distribution of the C-$LiFePO_4$ particles were firstly analyzed by powder XRD. The XRD pattern was showed in Fig. 1, it is revealed that all diffraction peaks were indexed and matched well with the standard diffraction data for orthorhombic phase $LiFePO_4$ with a phospho-

olivine structure (P_{nma}, JCPDS No. 83-2092), which indicates that the particles crystallized in a single phase structure. No crystalline carbon phase can be identified from the XRD pattern, indicating that the existed carbon is amorphous and very low; and its presence does not influence the olivine structure of $LiFePO_4$.

It was noted that very small amount of impurity phase is also present, which can be identified as Li_3PO_4 in the XRD pattern. Nevertheless, such as minor impurities could have been induced during the calcinations process in the highly reducing environment. Instead, such like the impurity phase was reported to have somewhat benefits for fast charging and discharging by providing a guest ion-conductive surface [20, 25].

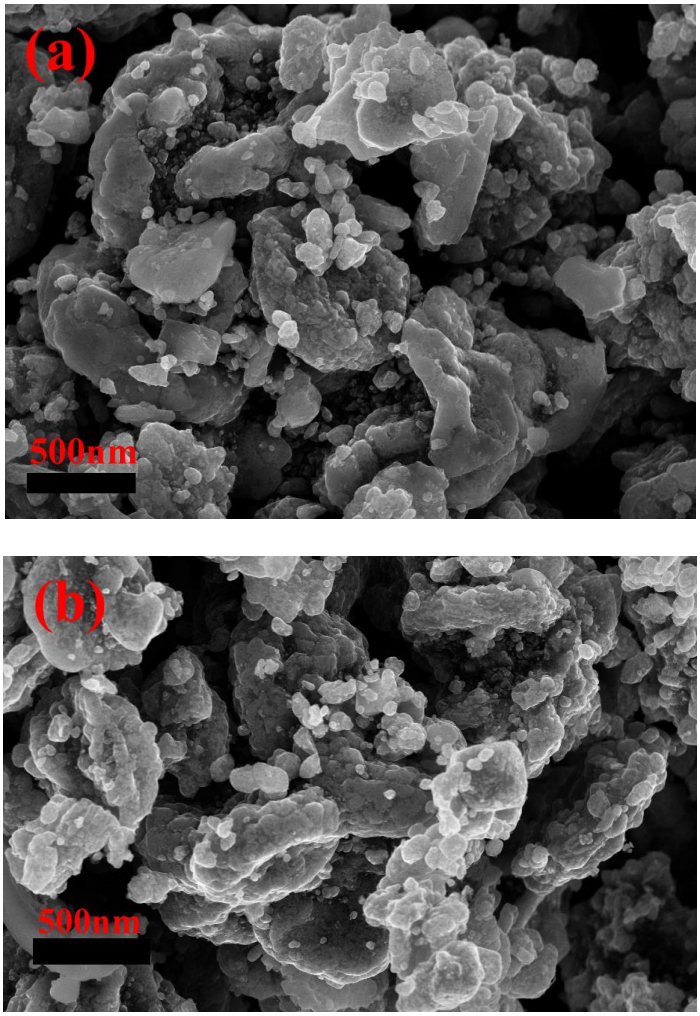

Figure 2 (a, b). Two representative FE-SEM images of as-prepared C-$LiFePO_4$ nanocomposites

The peaks of (101), (111)/(201), (211)/(020), and (311) in the XRD pattern were selected to calculate average particle sizes using the Scherrer's formula ($D = 0.9\lambda/\beta\cos\theta$, where λ = 0.1542 nm (Cu Kα) and β = full width half maximum at the diffraction angle of θ), the estimated average size was calculated between 50 nm and 85 nm. The least squares fit of the XRD data also yielded lattice parameter values of a=1.033 nm, b=0.603nm, and c=0.469 nm, which is comparable to the unit-cell

parameters of Olivine $LiFePO_4$ structure (P_{nma}) [1-5]. Indeed, the particle size can be controlled by heat treating at different temperatures.

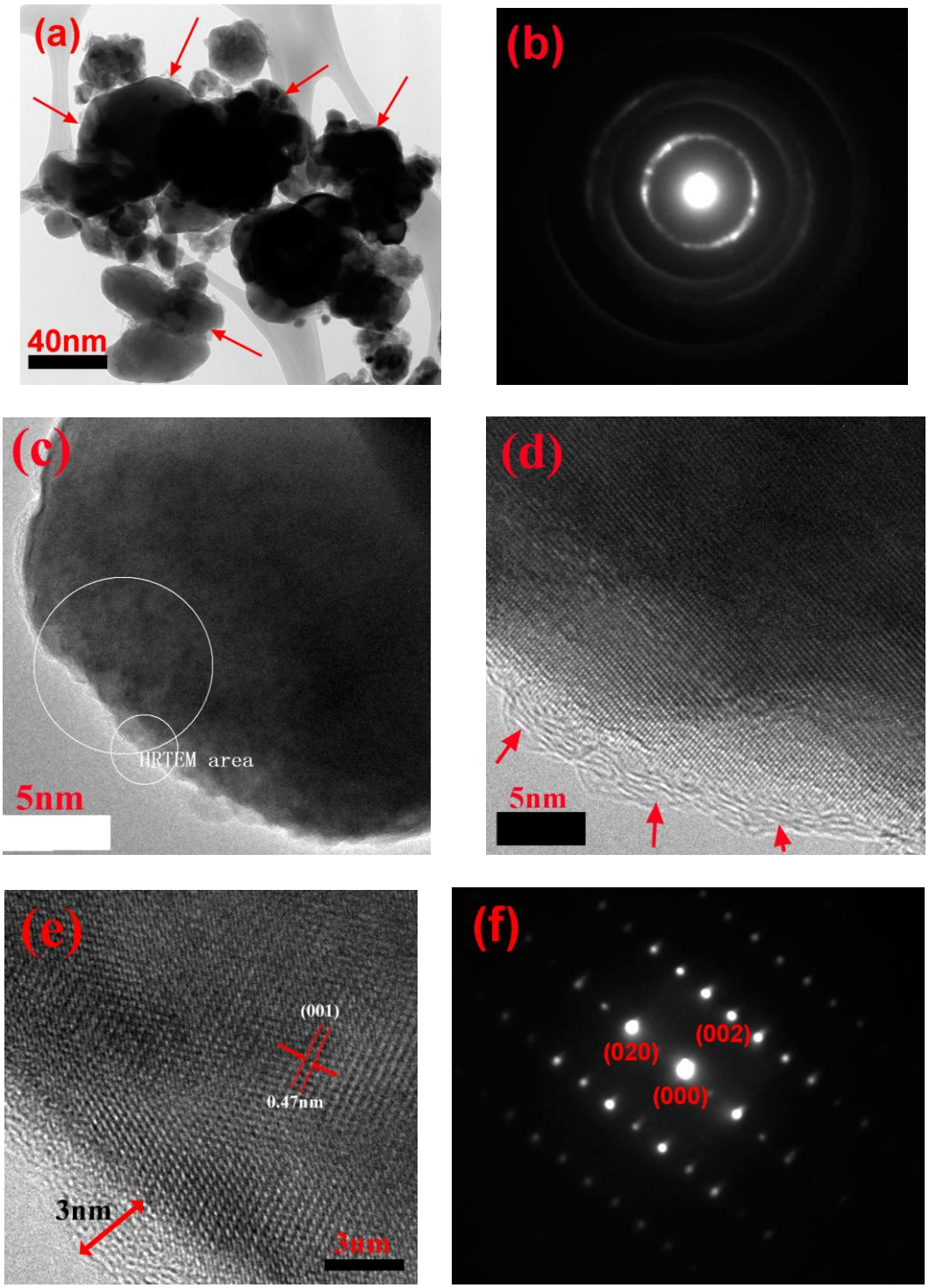

Figure 3. Typical BF-TEM images of C-$LiFePO_4$ particles (**a, c**) and HR-TEM images (**d, e**) and SAED patterns (**b, f**) Note: single Olivine phase and amorphous carbon coating layer are clearly observed

Surface morphologies of the C-$LiFePO_4$ nanocomposites particles were subsequently characterized by FE-SEM imaging. Two representative SEM images are illustrated in the Fig. 2 (a, b), it can be seen that most C-$LiFePO_4$ exhibited non-uniform fine particles assemblies that agglomerated each other, and the highly irregular aggregates are having a size distribution approximately between 500 nm and 1 μm. It is worth mentioning that the C-$LiFePO_4$ exhibited small adherence to the surface, which appeared to be conductive carbon. It was considered that the surface carbon adherence suppressed particle growth during calcinations preparation. Actually, those particles are adequately stable; consequently, they cannot be disrupted into fragments easily. In addition, average carbon content of particle aggregates is measured around as 4.2% (mass fraction) from the quantitative energy-dispersive X-ray micro-analysis (SEM/EDX).

Fig. 3(a) displays a typical bright-field TEM image (BF-TEM) of the C-$LiFePO_4$ nanocomposite particles. It is apparent that the particles show a rough spherical shape with the sizes ranging order of 50-100 nm, which is consistent with the XRD calculation. The appearance of distinct and diffuse SAED rings at Fig. 3(b) obtained from the particles shown in Fig.3 (a) revealed the co-existence of an amorphous and the crystal phase in the C-$LiFePO_4$ particles. The HR-TEM images of Fig. 3 (d) and Fig. 3(e) further give more insights into the morphologies of C-$LiFePO_4$ particles. It is clearly visible that an amorphous carbon layer covered the surface of $LiFePO_4$, which in the interstitial particle/boundary region as marked by red arrows. It has been found that formation of an amorphous carbon in the surface of the particles is attributed to the nature of carbon sources during solid-reaction, and was generated by carbonization of the conductive carbon precursors [19, 23, 26, 27]. Meanwhile, it is observed that the coating seems to be continuous and uniform with a thickness of 3 nm, suggesting that the carbon precursors also played an important role in reducing the $LiFePO_4$ particle size during high-temperature calcinations. The similar results of the amorphous carbon coating that inhibits grain growth were also reported by other groups [19, 26, 27]. The well-resolved lattice fringes showed in Fig. 3(d) and Fig. 3(e) simultaneously demonstrate the highly crystalline and single-crystal feature of the $LiFePO_4$ structures. The typical d-spacing of 0.47 nm as marked in Fig. 3(e) is consistent with the (001) plane of the orthorhombic structure of $LiFePO_4$. The corresponding SEAD pattern in Fig. 3(f) taken from the individual particle of HR-TEM image of Fig. 3(e) also demonstrates the single-crystal nature of the $LiFePO_4$. The indexing of electron diffraction spots correspond to the (020) and (002) planes of $LiFePO_4$ crystals, which further revealing the single-crystalline olivine-phase has been formed during solid state reaction. Similarly, average carbon mass content was also measured as 4.15% by EDX chemical probing analysis along with the HR-TEM images, which matched well with the above SEM/EDX data.

Energy filtered TEM (EF-TEM) imaging was performed to further investigate carbon coating framework and local surface state of the C-$LiFePO_4$ particles. The BF-TEM image of representative particle is selected and showed in Fig.4(a). The elemental compositional imaging analysis was carried out throughout the particle; the resulting elemental distribution mapping was showed in Fig. 4(b). Apparently, this is a typical core-shell particle structure, demonstrating the well-defined evidence of a thinner carbon coating layer completely covering the exposed $LiFePO_4$ particle surfaces that observed from the unique carbon (C) and ion (Fe) elemental mappings distributed with different colors in the

Fig. 4(b), which is in well accordance with the above HR-TEM images observations and SAED analysis.

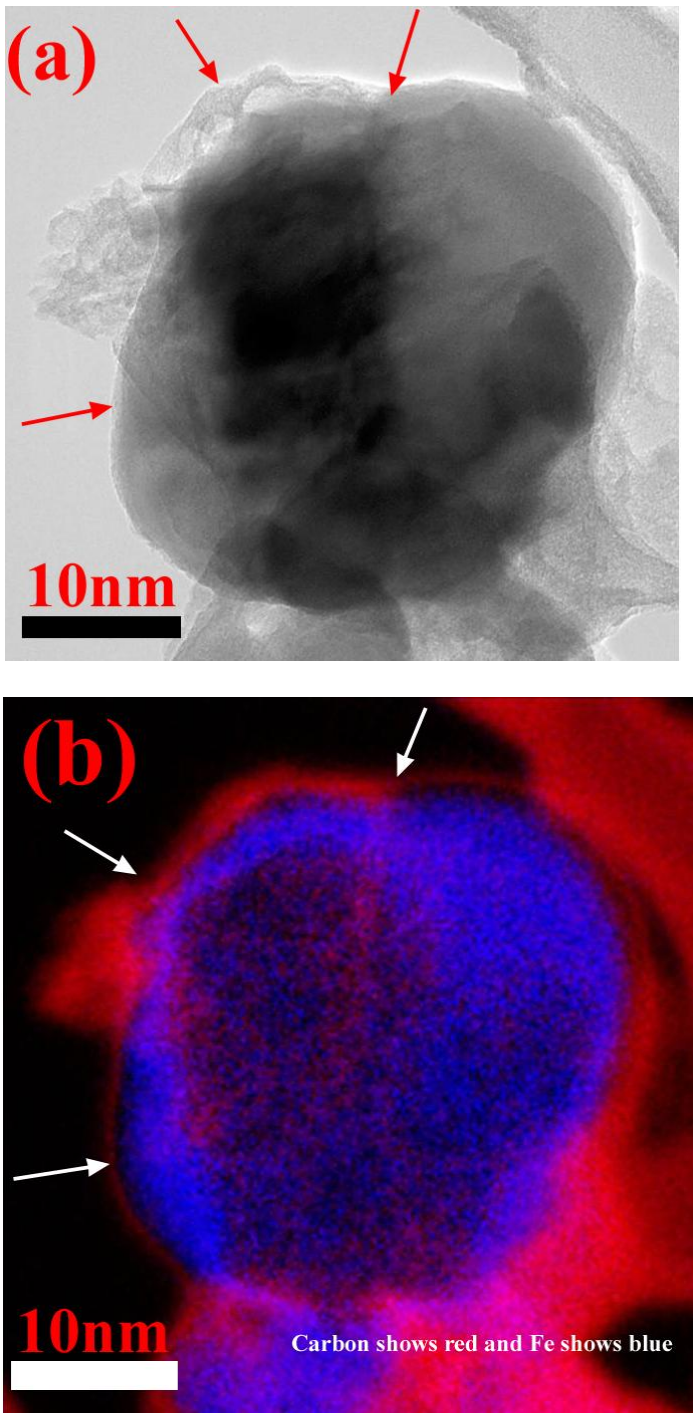

Figure 4. Typical BF-TEM image of individual C-$LiFePO_4$ particle (**a**). The energy-filtered TEM (EF-TEM) image and elemental map (**b**)

It is can be concluded that, structural analyses of HR-TEM imaging and EF-TEM imaging convincingly reveal that the formation of a stable phospho-olivine C-$LiFePO_4$ nanocomposite particle,

each particle has a single-crystal $LiFePO_4$ core and a thinner carbon coating layer, which is also in good agreement with the morphological details that reported for carbon-coated lithium metal phosphate previously [26-30].

3.2. STEM-HAADF imaging and EELS analysis

Scanning transmission electron microscopy high-angle annular dark field (HAADF) imaging and EELS spectra was employed to further visualize the C-$LiFePO_4$ particles, since the combinational technique is able to probe the chemical and valence states along the particles at the nano-scale [31, 32]. It is well known that elemental valence band excitations and phase compositions of the transition-metal can be feasibly detected and determined at nanometer resolution from the analysis of energy loss near edge structures (ELNES) in a typical EELS spectra [31, 32]. Particularly, it is well recognized that the EELS edge spectra is proven to be a very powerful tool for studying nano-structured $LiFePO_4$ because the valence state of the transition Fe metal can be analyzed by measuring the relative intensity of the Fe L_3 and Fe L_2 lines [31-33].

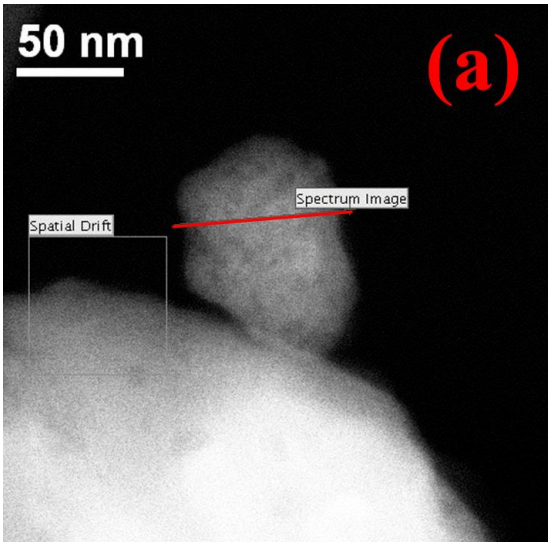

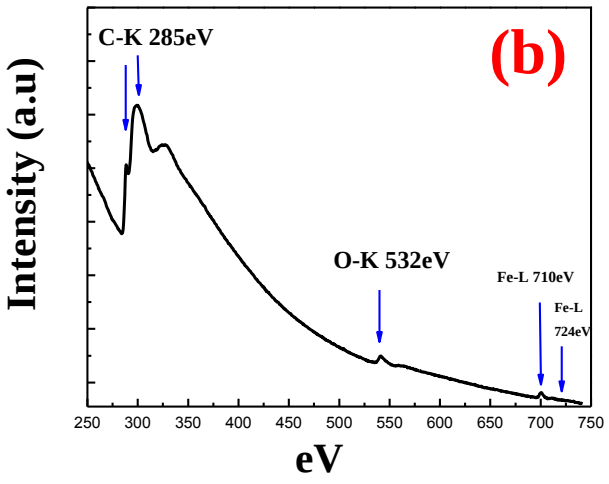

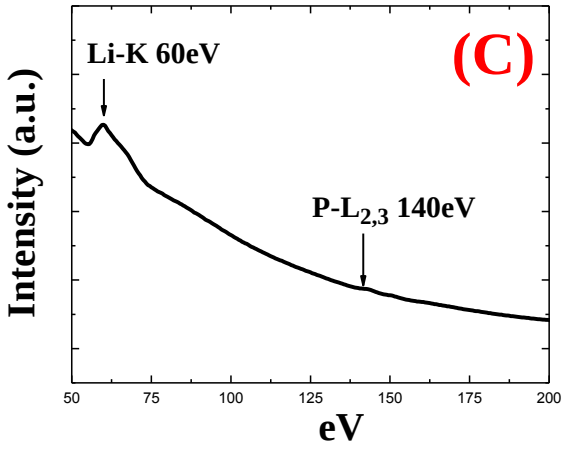

Figure 5. Typical STEM-HAADF image (**a**) and the EELS Spectra (**b**,**c**) for C-$LiFePO_4$ nanocomposite particles

A typical STEM-HAADF image of individual C-$LiFePO_4$ nanocomposite particles was showed in Fig. 5(a), the corresponding EELS spectra was recorded and showed in Fig. 5(b) and Fig. 5(c), respectively. First of all, the characteristics of the coating framework layer of C-$LiFePO_4$ particles surface were clearly identified in the EELS spectrum shown in Fig. 5(b). Obviously, the coating layer was proven to be sp2-bonded amorphous carbon by a C–K edge with maximum peak at 285.0 eV due to the C 1s→ π^* transition for disordered carbon-carbon sp2-hybridized bonds. Meanwhile, Fig. 5(b) shows Fe $L_{2,3}$ white lines recorded at high-loss energy range. In fact, the ELNES spectrum of the Fe–$L_{2,3}$ edge analyses in Fig. 5(b) was ascribed to the characteristics of Fe^{2+} in olivine $LiFePO_4$ structure. On the other hand, the Fe^{2+} valence state was appeared in the hybridization of P 3p states with the Fe 3d states occurred due to the FeO_6 octahedral site in olivine-$LiFePO_4$ structure, which is demonstrated by an L_3 edge peak maximum at 710 eV. It is also evident in Fig. 5(b) that O is determined by a O–K edge with a maximum peak at 532 eV, and that P is present in Fig. 5(c) by a P–$L_{2,3}$ edge with a double peak and a first maximum at 140 eV. Consequently, such like the O-K edge and P–$L_{2,3}$ edge is therefore inferred from the oxo-anions of $(PO_4)^{3-}$ unit, which is ascribed from the phospho-olivine structure of lithium transition-metal phosphates in the orthorhombic P_{nma} space group system [1, 31]. Specifically, it is well documented that the Li–K near edge structure is clearly visible and indentified in Fig.5(c). Indeed, the ELNES of Li with a K-edge at a maximum peak of 58 eV in the low energy core loss spectrum can be used as a fingerprint [31] for phase identification of LiO_6 octahedral sites located in olivine-structure of $LiFePO_4$.

3.3 Crystal structure by XPS analysis

As a powerful surface analysis technique, X-Ray photoelectron spectroscopy (XPS) has been well-suited for the evaluation of valence and electronic states of metal/non-metal ions, and extensively used in the characterizations of the olivine $LiFePO_4$ cathode materials [34-37].

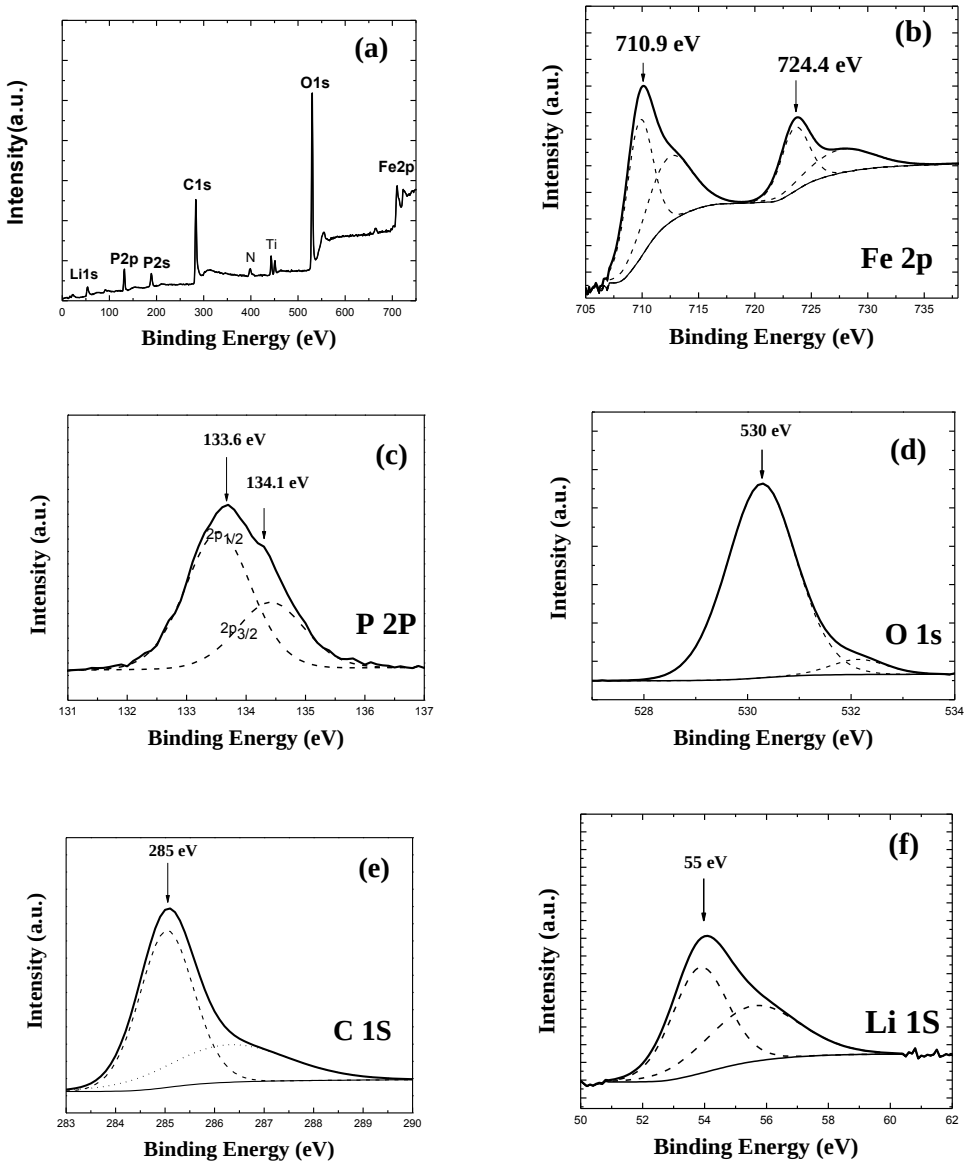

Figure 6. (**a**) is XPS spectrum survey profile of the C-$LiFePO_4$ nanocomposites particles. (**b-f**) is the core-scan XPS spectra of Fe2p, P2p, O1s, C1s, and Li1s profiles, respectively

The XPS spectrum survey profile and core-scan XPS spectra of Li 1s, Fe 2p, P 2p, O 1s, and C 1s profiles for the C-$LiFePO_4$ nanocomposites particles are shown in the Fig. 6(a) and Fig. 6 (b, c, d, e, f), respectively. It is clear that the survey profile in Fig.6 (a) shows that the main binding energy (BEs) of Li 1s, Fe 2p, P 2p and O 1s, C 1s peaks are determined to be 55 eV, 710 eV, 133 eV, 531 eV, and 285 eV, respectively. Here the Ti and N peaks were from the sample holder.

It is seen from Fig. 6(b) that the Fe 2p spectrum split into $2p_{1/2}$ and $2p_{3/2}$ due to the spin-orbit coupling. Each part consists of a main peak and a corresponding satellite peak at BEs of 710.9 and 724.4 eV for Fe $2p_{3/2}$ and Fe $2p_{1/2}$, respectively. In fact, the appearance of satellite peaks or shoulder peaks is a typical characteristic feature of transition metal ions with partially filled d-orbits [34]. Here,

the two distinct BEs peaks are attributed to the characteristic of the valence of the Fe^{2+} state in the $LiFePO_4$ olivine-structure as reported previously [34-38].

Meanwhile, the P 2p spectrum in Fig. 6(c) can be de-convoluted into two components of $2p_{3/2}$ and $2p_{1/2}$ at BEs of 134.1 eV and 133.6 eV due to spin–orbit coupling. The presence of only one doublet reveals the P chemical state should be the PO_4^{3-} tetrahedral group characteristic appeared in the lithium transition-metal phosphates, which indicating the absence of iron phosphides, thereby also further excludes the formation of impurity phases such as Fe_2P or Fe_2O_3 that appears at a BE value of 129.5 eV.

The O 1s spectrum in Fig.6 (d) has the main binding energy of 530 eV, which represents the oxide ions of PO_4^{3-} group existed in $LiFePO_4$. It has been proposed that the O 1s spectrum and P 2p spectrum exhibited the BE peaks at 530 eV and 133.6 eV are eventually originated from the phosphate units structure [34-38].

The main BE peak of 285 eV of C1s spectrum in Fig. 6(e) is clearly assigned to amorphous (284.7 eV) carbon with sp^2 C−C bonds, and such a BE value of C1s is consistent with the one reported from the literature [36-38]. The smaller difference for the reported binding energy (284.7 eV) is probably due to oxygen-containing surface functional groups formed at the surface because of air exposure. Anyway, the presence of an amorphous sp2-bonded carbon coating on the sample surface was revealed. Furthermore, it was showed that the centered BE peak of 55 eV in the Li 1s spectrum of Fig. 6(f) is also consistent with the BE value of Li^+ ions in the reported Olivine-$LiFePO_4$ cathode [34].

Therefore, the XPS analysis convincingly confirms the existence of Olivine phase purity and amorphous carbon phase in the C-$LiFePO_4$ nanocomposites, which is in well agreement with the above XRD data, HR-TEM images, EF-TEM images, and EELS analysis.

In a word, our successful synthesis of stable amorphous carbon-coated $LiFePO_4$ nanocomposites particles is obviously demonstrated.

3.4 Electrochemical performance studies

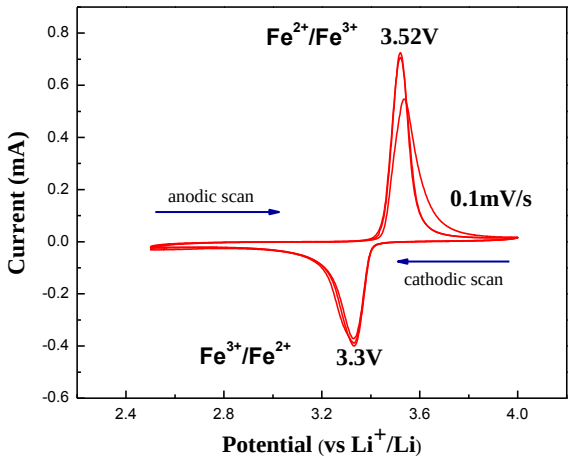

Figure 7 (a). The cyclic voltammetry (CV) profile was performed by the scan rate of 0.1 mV/s

The cyclic voltammogram (CV) at 0.1 mV/s using a charged coin cell within a potential window of 2.0-4.5 V (vs. Li/Li^+) is shown in Fig. 7(a). It is clear that C-$LiFePO_4$ showed one distinct anodic peak (charge) and cathodic peak (discharge). The well-defined sharp redox peaks in the range of 3.3-3.6 V should be attributed to the Fe^{2+}/Fe^{3+} redox couple reaction. The anodic peak at 3.52 V corresponded to the oxidation of Fe^{2+} to Fe^{3+}, and the reduction of Fe^{3+} to Fe^{2+} appeared at 3.3 V, which also corresponds to Li ions extraction and insertion in $LiFePO_4$ crystal structure. These are consistent with a two-phase redox reaction at about 3.5 V vs. Li/Li^+ [1-3]. This also implies that a two-phase Fe^{3+}/Fe^{2+} redox reaction proceeds via a first-order transition between $FePO_4$ and $LiFePO_4$ [1-3]. The CV profiles almost overlap after three cycles, revealing very good reversible kinetic reaction, In additions, sharp redox peaks and smaller potential interval peaks shown in the Fig. 7(a) demonstrated that lithium ions and electrons were quite active during kinetic redox reactions, which could be attributed to the smaller particles that reduced the diffusion length of the Li^+ ions, and the amorphous carbon-coating layer that facilitated the electrons transfer in C-$LiFePO_4$. It is also worth mentioning that the intensity and shape of the peak current in the CV profiles can be affected by carbon coating [7-19]. The C-$LiFePO_4$ electrode showed a higher peak current than the no-coated $LiFePO_4$, demonstrating that both Li^+ ions and electrons considerably contributed to kinetic redox reactions as a result of the carbon coating on $LiFePO_4$.

Fig. 7(b) shows the brief schematic diagram of Li^+ ions intercalation/de-intercalation processing during charge-discharge of the $LiFePO_4$ nanocomposites. One of the fascinating characteristics of $LiFePO_4$ is its ability to be used at very high cycling rates, although it does exhibit lower electronic conductivities. So far, based on many research efforts focused on neutron diffraction data, electron microscopy/electron energy loss spectroscopy observations, and theoretical simulations, several reasonable models have been proposed to establish the relation between the structure and both ionic and electronic transport properties of $LiFePO_4$ cathode materials [39-44].

An earlier model proposed the reversible charge/discharge (de-lithiation/lithiation) of Olivine $LiFePO_4$ to be a two-phase transition reaction by $FePO_4 + xLi^+ + xe^- = xLiFePO_4 + (1-x)\ FePO_4$ [39]. The shrinking-core model was proposed to explain the behavior of $LiFePO_4$ electrodes with an isotropic core-shell mechanism [40, 41]; however this model didn't consider the microscopic process involved during the reaction. The macroscopic domino-cascade model mechanisms at the nanoscale level [42, 43] well explained how Li^+ ions and electrons can move as solid-solution reactions inside the olivine $LiFePO_4$ structure particles.

To understand the whole lithium de-intercalation /intercalation mechanism, the ionic and the electronic conductivities needed to be considered simultaneously, as both processes are coupled at the microscopic scale; the effect of strong local distortions must also be account for. As reported [43], the major drawback of the shrinking-core and core−shell models to describe the evolution of the reaction mechanisms observed experimentally is the necessity for the majority of particles to be at similar degrees of lithiation. However the most $LiFePO_4$ particles have a distribution of sizes, so it is unlikely that the majority of particles meet this requirement.

In fact, $LiFePO_4$ functions/works as a cathode where de-lithiation (charge) occurs via either a solid-solution or a two-phase mechanism, which is influenced by sample preparation and electrochemical conditions. The reaction mechanism is found to be also affected by particle size,

which determines whether two-phase reactions can be stabilized within a particle. It is interesting to note that the core-shell models and domino-cascade models have been verified to describe different experimental observations, which indicated the domino-cascade model explains the mechanism at the particle scale, but the core-shell models are valid at an agglomerate (meso) scale [43].

The direct experimental evidence for competitive solid-solution and two-phase reactions occurring within a $LiFePO_4$ cathode under non-equilibrium conditions was also revealed [44], as theoretically predicted [45]. The simultaneous occurrence of solid-solution and two-phase reactions can be confirmed by in situ neutron powder diffraction after deep discharge at non-equilibrium conditions.

As mentioned earlier [1-10], the $LiFePO_4$ lattice is an assembly of FeO_6 octahedra sharing corners and forming Fe-O atomic *ac* planes. The tetrahedral PO_4 units link these planes together, which forms the skeleton of the lattice. The presence of one common edge between each PO_4 tetrahedron and each FeO_6 octahedron in the $LiFePO_4$ lattice is very particular. The mobile Li^+ form one dimensional chains in the structure that run parallel to planes of corner-shared FeO_6 octahedra, and along the [010] direction in the orthorhombic P_{nma} lattice. This generates preferential rapid one-dimensional Li^+ ion conductivity along that direction. But the strong covalency of the P–O bond is found in phosphates. Therefore, in the olivine structure, this edge-sharing induces strong distortions at the local scale that spread in a cooperative way through all of the crystallite.

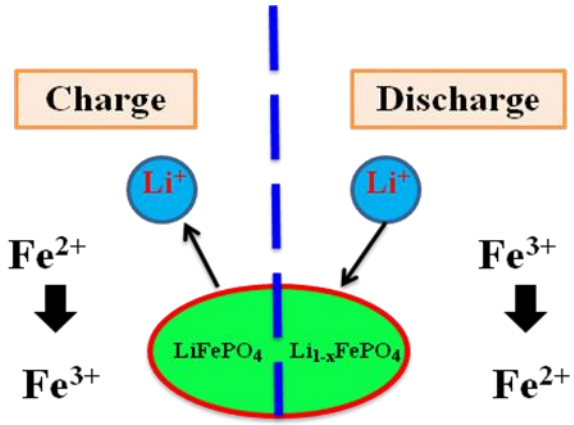

Figure 7 (b). Schematic diagram of Li ion intercalation/de-intercalation processing during charge-discharge for the $LiFePO_4$

In particular, during lithium de-intercalation, Fe^{2+} ions are oxidized to Fe^{3+} with strong changes in the Fe–O bond lengths and O–O distances in FeO_6 octahedra, leading to a cooperative structure distortion. Overall, these structural distortions have a significant impact on the electronic conductivity. The very high concentration of Li^+/vacancies and Fe^{2+}/Fe^{3+} polarons localized in this interfacial zone enables a very fast reaction. This interfacial zone is unstable and can move very rapidly inside the crystallite, like a wave going through the particle in the *a* direction on de-intercalation /intercalation processing [42]. Recently, the first-principles calculation result demonstrated the critical effects of the local crystal structure changes on the electronic structure and the kinetic properties of Olivine cathodes

due to both Li^+ ion mobility and electron conductivity are significantly enhanced by the local structure change [46].

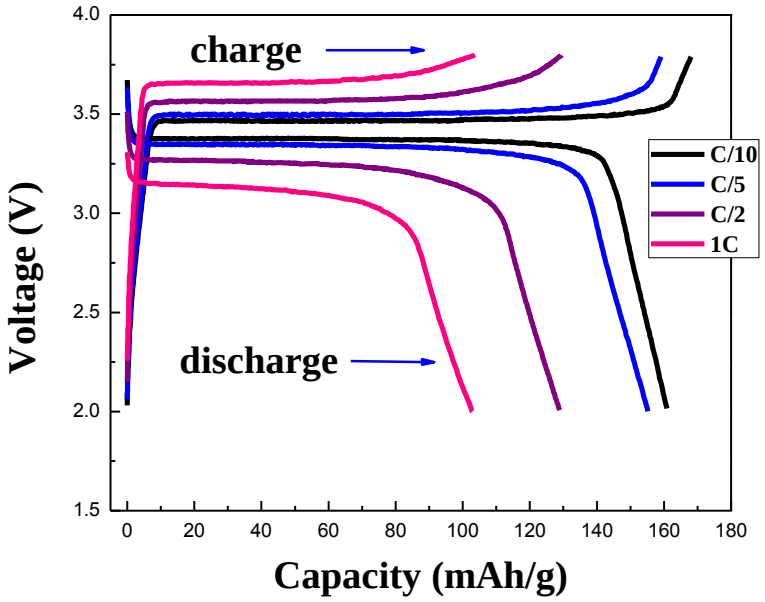

Figure 8. The discharge and charge profiles of C-$LiFePO_4$ nanocomposites at different current rates

In order to evaluate the electrochemical cycle capability performance for the C-$LiFePO_4$ nanocomposites, galvanostatic discharge-charge cycling testing, at various current densities of C/10, C/5, C/2, 1C, was performed at different cycles and showed in Fig. 8. The cell exhibited a typical plateau at 3.42 V (versus Li^+/Li) associated with the Fe^{3+} to Fe^{2+} redox process for the $LiFePO_4$ electrodes. It is clear from the Fig. 8 that the C-$LiFePO_4$ nanocomposites delivered almost 99% of their theoretical discharge capacity of 168 mAh/g at C/10 rate. The exceptionally high capacity is due to full usage of the active material at C/10 rate.

Also the good discharge capacity retention of approximately 165 mAh/g at C/5, 140 mAh/g at C/2 and 115 mAh/g at 1C were achieved after charging/discharging cycle, respectively. Very good reversible charge–discharge symmetry from C/10 to 1C was observed, which also demonstrates less polarization during the galvanostatic discharge-charge cycling. That is attributed to the nanometer particles and carbon-coating network that enables both Li^+ ions and electrons to migrate and reach each of the nanocomposite particles, hence facilitating the more potential usage of the active materials. Which is in good agreement with the CV results shown in Fig.7(a).

Fig.9 is the rate capabilities performance for C-$LiFePO_4$ nanocomposites electrode cycled at different current rates from C/10 to 20C**.** No obvious decline was observed in the discharge capacity that remained stable during every cycling, and the good rate performance is revealed, and a better lithium intercalation/de-intercalation property is demonstrated.

However, it should be noted that the discharge capacity becomes low at a high current density (e.g., 5C, 10C, 20C), which can be ascribed to the slowing diffusion of Li^+ ions inside particles at high

current rates, consequently leading to the low Li^+ storage capability as a result of insufficient usage of the active electrode materials.

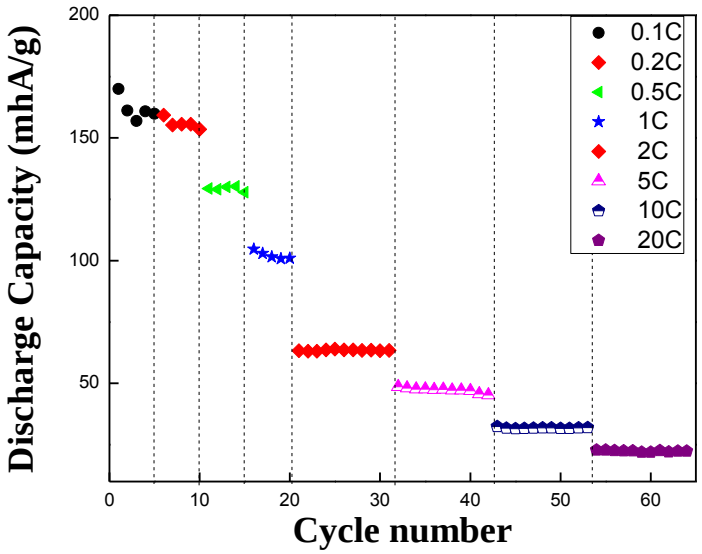

Figure 9. The rate capabilities for C-$LiFePO_4$ nanocomposites at different current rates (from 0.1C to 20C)

This indicated that our C-$LiFePO_4$ nanocomposites demonstrated the superior discharge capacity and good rate capability, and cycling performance with initial discharge capacities 168 mAh/g at C/10. As we already discussed, these improved properties were significantly correlated to the improved electronic conductivity of the $LiFePO_4$ coated with amorphous carbon and smaller charge transfer resistance as shown in the following electrochemical impedance spectroscopy data. As also mentioned earlier, the active materials with better electronic conductivity should have better discharge capacity and cycling capabilities. It is believed that the crucial role played by the surface carbon-coating on the C-$LiFePO_4$ nanocomposites is responsible for the better electrochemical high power performance due to the effective increase of both electronic and ionic transport.

To the best of our knowledge, much effort has been made to improve high power performance of $LiFePO_4$ cathode by carbon coating to increase its surface conductivity [47-54]. Surface carbon coating has been well recognized as an alternative to enhance surface electronic conductivity in the design of a cell battery electrode. The significant role of the carbon layer is believed to be creating a better electric contact between the intra-particles inside the Li-ion cell. Once an electron has arrived at the surface of the particle it can migrate to the collector of the electrode rapidly through the connected network of conductive carbon. Moreover, the non-coated $LiFePO_4$ cathode particles have a disordered surface layer [47], which results in an increased electric resistance of battery cells. The full carbon coating is also expected to cure the structural disorder on each particle surface, thus reducing the electric resistance in the surface of particles. Another significant influence, reported from several research groups [49-54], is that the carbon layer permits the pass of Li^+ while preventing the pass of solvent molecules of the electrolyte during the Li-intercalation process; the carbon layer plays the role

of a buffer layer on Li-intercalation, which may improve the adsorption of Li^+ and mobility of Li^+ on the outer surface of $LiFePO_4$ [8, 49] used in the battery cell.

It is still unclear whether the carbon coating improves interfacial charge transfer in the $LiFePO_4$ cathode, which may be another specific reason for the high power performance. It should be further investigated with more advanced surface analysis technology [8, 49]. Meanwhile, the synergetic effects of carbon coating of the creation of the Fe^{2+}/Fe^{3+} polarons and improved interfacial charge transfer also need to be further confirmed.

To understand carbon coating effect intensively, electrochemical impedance spectroscopy (EIS) was measured on the CR-2032 coin cells in the fully charge state at the frequency range between 100 kHz and 10 mHz. Before EIS test, the cells were subjected to charge and discharge for three cycles to guarantee the penetration of electrolyte and formation of active layer. Fig.10 represents the Nyquist plot from EIS measurement for the charged C-$LiFePO_4$ electrode cell. The plot has an intercept at high frequency, followed by a semicircular plot in the medium-to-high frequency region and a sloping line in the low frequency region.

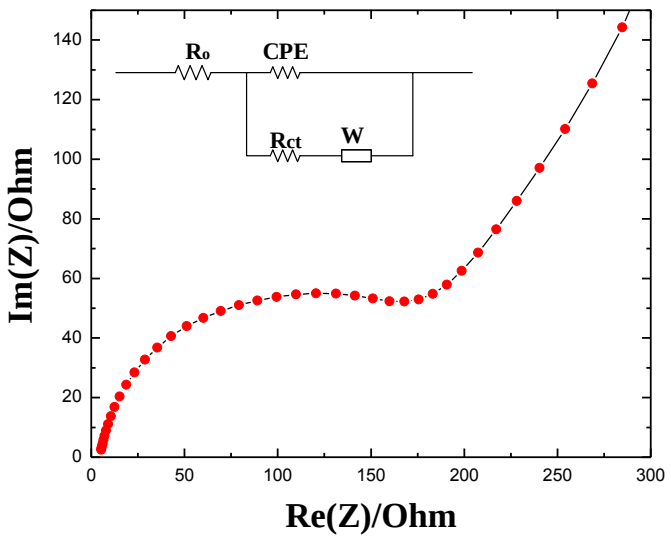

Figure 10. The Nyquist plot from EIS measurement for the charged C-$LiFePO_4$ electrode cell at the frequency range of between 100 kHz and 10 mHz. The equivalent circuit model is shown in the inset

The intercept at the Re(Z) axis in the high frequency region was attributed to the ohmic resistance (R_e), representing the resistance of the electrolyte. The semicircular plot in the medium frequency range is associated with the charge transfer resistance (R_{ct}) of the electrochemical reaction, and the sloping line in the low frequency region represents the diffusion of lithium ions into the bulk of the cathode material, namely the Warburg impedance [55, 56]. This is because the Warburg impedance at low frequency is directly related to the lithium-ion diffusion process in an electrode material.

Such an EIS spectra data can be fitted by an equivalent circuit model as shown in the inset of Fig.10. It was revealed that the R_{ct} value for the C-$LiFePO_4$ nanocomposites is calculated to be around 110 Ω. It is clear that the R_{ct} values are lower than several literature values [57-60]. Generally, the

value of R_{ct} is small enough to force Li^+ ions and electrons react immediately, accelerating the transport of the polarons of Li^+ ions and electrons at the electrode, which is beneficial to the kinetic reactions during charge-discharge process. As a result, the electrochemical performance is improved. This also demonstrates that the EIS is completely consistent with the results from the CV and the cycling testing.

4. CONCLUSIONS

In summary, amorphous carbon-coated $LiFePO_4$ (C-$LiFePO_4$) nanocomposites particles have been scale-up synthesized in larger commercial productions. The state-of-the-art techniques of structural analysis such as TEM, HR-TEM, EF-TEM, STEM-HAADF, EELS spectroscopy and XPS spectroscopy provide a comprehensive view of the structure-performance correlation of C-$LiFePO_4$ particles, and clearly demonstrate the well-ordered Olivine $LiFePO_4$ crystal covered with uniform and thinner carbon layers. In particular, both XPS spectra and EELS spectra analysis further confirmed the amorphous sp2 bonded carbon-coating nature. It is very evident that the uniform carbon coating on the surface of each $LiFePO_4$ particle creates effective pathway networks for both electronic transport and ionic diffusion during the electrochemical testing, and thereby enhances the electronic conductivity and its electrochemical performance.

All the satisfied prerequisites for generating good rate capability, cycling performance, and high discharge capacity for those C-$LiFePO_4$ nanocomposites, should enable the development of long-life lithium batteries in terms of stability (non-volatile), safety (non-explosive) and high energy density suitable for both plug-in hybrid and all-electric vehicles. Our present technique is also very useful to optimize for mass commercial production of the C-$LiFePO_4$ materials; since this method is likely to be easy to scale up for industrial production. Meanwhile, the full structural observations and evaluations are also helpful to guide the general understanding of how to produce high-quality C-$LiFePO_4$ cathode in relevance to lower energy consumption and low-cost appropriate precursors.

ACKNOWLEDGEMENTS

The Postgraduate Scholarships from the Natural Sciences and Engineering Research Council of Canada (NSERC) and the President's Award of University of Waterloo are greatly appreciated by XC Sun. The supports from JiangSu Province Double Talents Promotion Plan and JiangSu Fangzhou New-Energy Company at China are greatly grateful. Thanks to Prof. Yuefei Zhang and Prof. Jinbo Yang on the kind helps in the XRD analysis and SEM imaging at Beijing University of Technology and Beijing University in China. Thanks to Prof. Jie Shu at NingBo University in China and Prof. Xueliang Sun at University of Western Ontario for their stimulating discussions.

References

1. A. K. Padhi, K. S. Nanjundaswamy, J. B. Goodenough, *J. Electrochem. Soc*., 144 (1997) 1188
2. M. Thackeray, *Nature Mater*., 1 (2002) 81
3. S.-Y Chung, J. T. Bloking, Y.M. Chiang, *Nature Mater*., 1 (2002) 123
4. C. A. J. Fisher, V. M. Hart Prieto, M. S. Islam, *Chem. Mater*., 20 (2008) 5907
5. V.T. Indrajeet, V. Mathur, N. H. John, D. R. Wheeler, *J. Power Sources*, 162 (2006) 673

6. J. M. Tarascon; N. Recham, M. Armand, J. N. Chotard, P. Prabanda, W. Walker, L. DuPont, *Chem. Mater*., 22 (2010) 724
7. H. Huang, S. C. Yi, L. F. Nazar, *Electrochem. Solid State Lett*., 4 (2001) A170
8. Y. Wang, P. He, H. Zhou, *Energy Environ. Sci*., 4 (2011) 805
9. S. Y. Chung, Y. M. Kim, S. Y. Choi, *Adv. Funct. Mater*., 20 (2010) 4219
10. N. Recham, J.N. Chotard, L. Dupont, C. Delacourt, W.Walker, M. Armand, J-M. Tarascon, *Nature Mater*., 9 (2010) 68
11. a) G. T. K. Fey, T. L. Lu, *J. Power Sources*, 178 (2008) 807. b) Z. G. Lu, H. L. Chen, R. Robert, Y. X. Zhu, J. Q. Deng, L. J. Wu, C. Y. Chung, C. P. Grey, *Chem. Mater*., 23 (2011) 2848
12. a) M. Maccario, L. Croguennec, F. Le Cras, C. Kelmas, *J. Power Sources*, 183 (2008) 411. b) K. T. Lee, J. Cho, *Nano Today*, 6 (2011) 28
13. A. Yamada, S. C. Chung, K. Hinokuma, *J. Electrochem. Soc*., 148 (2001) A224
14. M. Piana, B.L. Cushing, J. B. Goodenough, N. Penazzi, *Solid State Ionics*, 175 (2004) 233
15. G. Meligrana, C. Gerbaldi, A. Tuel, S. Bodoardo, N. Penazzi, *J. Power Sources*, 160 (2006) 516
16. D. Choi, P. N. Kumta, *J. Power Sources*, 163 (2007) 1064
17. S. B. Lee, S. H. Cho, S. J. Cho, G. J. Park, S. H. Park, Y. S. Lee, *Electrochem. Commun*., 10 (2008) 1219
18. J. C. Zheng, X. H. Li, Z. X. Wang, H. J. Guo, S. Y. Zhou, *J. Power Sources*, 184 (2008) 574
19. Y. G. Wang, Y.R. Wang, E. Hosono, K.X. Wang, H. S. Zhou, *Angew. Chem. Int. Ed*., 47 (2008) 7461
20. a) B. Kang, G. Ceder, *Nature*, 458 (2009) 190. b) G. Ceder, B. Kang, *J. Power Sources*, 194 (2009) 1024
21. J. J. Wang, X. L. Sun, *Energy Environ. Sci*., 5 (2012) 5163
22. a) M. R Yang, W.H Ke, S.H Wu, *J. Power Sources*, 146 (2005) 539. b) Y.B. Xu, Y.J. Lu, L. Yan, Z.Y. Yang, R. D. Yang, *J. Power Sources*, 160 (2006) 570. c) Z.Y Chen, H.L. Zhu, S. Ji, R. Fakir, V. Linkov, *Solid State Ionics*, 179 (2008) 1810
23. O. Toprakci, H. A. K. Toprakci, L.W. Ji, X.W. Zhang, *KONA Powder and Particle Journal*, 28 (2010) 50
24. X.C. Sun, K. Sun, C. Y. Chen, H. P. Sun, B. Cui, *Int. J. Mater. Chem.*, 2 (2012) 218
25. a) G. X. Wang, H. Liu, J. Liu, S. Z. Qiao, G.Q. Lu, P. Munroe, H. J. Ahn, *Adv. Mater*., 22 (2010) 4944. b) S. Herle, B. Ellis, L. F. Nazar, *Nature Mater*., 3 (2004)147
26. M. M. Doeff, J. D. Wilcox, R. Kostecki, G. Lau, *J. Powder Sources*, 163 (2006) 180
27. J. D. Wilcos, M. M. Doeff, M. Marcinek, R. Kostecki, *J. Electrochem. Soc*., 154 (2007) A389
28. H. T. Kuo, T. S. Chan, N. C. Bagkar, R. S. Liu, C. H. Shen, D. S. Shy, X. K. Xing, J.F. Lee, *Electrochem. Solid State Lett*., 12 (2009) A111
29. S. W. Oh, S. T. Myung, H. J. Bang, C. S. Yoon, K. Amine, Y. K. Sun, *Electrochem. Solid State Lett*., 12 (2009) A181
30. J. Liu, T. E. Conry, X. Song, L. Yang, M. M. Doeff, T. J. Richardson, *J. Mater. Chem*., 21 (2011) 9984
31. a) P. A.V. Aken, B. Liebschen, V. J. Styrsa, *Phys. Chem. Miner*., 25 (1998) 323. b) F. Wang, J. Greatz, M. S. Moreno, C. Ma, L. Wu, V. Volkov, Y. Zhu, *ACS Nano*, 5 (2011) 1190
32. a) L. Laffont, C. Delacourt. P. Gibot, M. Y. Wu, P. Kooyman, C. Masquelier, J. M. Tarascon, *Chem. Mater*., 18 (2006) 5520. b) M. K. Kinyanjui, P. Axmann, M .W. Mehrens, P. Moreau, F. Boucher, U. Kaiser, J. Phys.*:* Condens. *Matter, 22* (*2010*) 295501
33. W. Porcher, P. Moreau, B. Lestriez, S. Jouanneau, D. Guyomard, *Electrochem. Solid State Lett*., 11(2008) A4
34. a) N. N. Sinha, C. Shivakumara, N. Munichandraiah, *ACS Appl. Mater. Interfaces*, 2 (2010) 2031. b) J. W. Zhang, L.H. Zhuo, L. L. Zhang, C.Y. Wu, X. B. Zhang, L.M. Wang, *J. Mater. Chem*., 21 (2011) 6975. c) M. M. Doeff, J. D. Wilcox, R. Yu, A. Aumentad, M. Marcinek, R. Kostecki, *J. Solid State Electrochem*., 12 (2008) 995

35. C. R. Sides, F. Croce, V. Y. Young, C. R. Martin, B. Scrosati, *Electrochem. Solid State Lett*., 8 (2005) A484
36. M. S. Bhuvaneswari , N. N. Bramnik , D. Ensling , H. Ehrenberg, W. Jaegermann, *J. Power Sources*, 180 (2008) 553
37. J. B. Lu, Z. L. Tang , Z. T. Zhang, W.C. Shen, *Mater. Res. Bulletin*, 40 (2005) 2039
38. F. Yu, J. J. Zhang, Y. F. Yang, G. Z. Song, *J. Mater. Chem*., 19 (2009) 9121
39. C. Delacourt, P. Poizot, J. M. Tarascon, C. Masquelier, *Nat. Mater*., 4 (2005) 254
40. a) V. Srinivasan, J. Newman, *Electrochem. Solid State Lett*., 9 (2006) A110. b) W. Sigle, R. Amin, K. Weichert, P. A. Aken, J. Maier, *Electrochem. Solid State Lett.*, 12 (2009) A151
41. B. Ellis, L. K. Perry, D. H. Ryan, L. F. Nazar, *J. Am. Chem. Soc*., 128 (2006) 11416
42. C. Delmas, M. Maccario, L. Croguennec, F. Le Cras, F. Weill, *Nat. Mater*., 7 (2008) 665
43. G. Brunetti, D. Robert, P. B. Guillemaud, J. L. Rouviere, E. F. Rauch, J. F. Martin, J. F. Colin, F. Bertin, C. Cayron, *Chem. Mater*., 23 (2011) 4515
44. N. Sharma, X.W. Guo, G. D. Du, Z. P. Guo, J. Z. Wang, Z. X. Wang, V. K. Peterson, *J. Am. Chem. Soc*., 134 (2012)7867
45. P. Bai, D. A. Cogswell, M. Z. Bazant, *Nano Lett*., 11 (2011) 4890
46. D. Seo, H. Gwon, S. Kim, J. Kim, K. Kang, *Chem. Mater*., 22 (2010) 518
47. K. Zaghib, A. Mauger, F. Gendron, C. M. Julien, *Chem. Mater*., 20 (2008) 462
48. a) C. M. Julien, A. Mauger, K. Zaghib, *J. Mater. Chem*., 21 (2011) 9955. b) Z. H. Li, D. M. Zhang, F. X. Yang, *J. Mater. Sci*., 44 (2009) 2435
49. R. Malik, A. Abdellahi, G. Ceder, *J. Electrochemical Society*, 160 (2013) A3179
50. M. L. Trudeau, D. Laul, R. Veillette, A. M. Serventi, A. Mauger, C. M. Julien, K. Zaghib, *J. Power Sources*, 196 (2011) 7383
51. C. M. Julien, A. Mauger, K. Zaghi, *J. Mater. Chem*., 21 (2011) 9955
52. F. Teng, S. Santhanagopalan, R. Lemmens, X. B. Geng, P. Patel, D. D. S. Meng, *Solid State Sci*., 12 (2010) 952
53. J. W. Fergus, *J. Power Sources*, 195 (2010) 939
54. B. Scrosati, J. Garche, *J. Power Sources*, 195 (2010) 2419
55. H. Liu, Q. Cao, L. J. Fu, C. Li, Y. P. Wu, H. Q. Wu, *Electrochem. Commun*., 8 (2006) 1553
56. J. Molenda, W. Ojczyk, J. Marzec, *J. Power Sources*, 174 (2007) 689
57. Y.W. Chen, J. S. Chen, *Int. J. Electrochem. Sci*., 7 (2012) 8128
58. S. C. Jheng, J. S. Chen, *Int. J. Electrochem. Sci*., 8 (2013) 4901
59. Z. Ma, G. J. Shao, G. L. Wang, J.P. Du, Y. Zhang, *Ionics*, 19 (2013) 437
60. J. J. Song, Y. Zhang, G. J. Shao, *J. Nanomaterials*, 2013 (2013) 687501